This is a preprint, the final version is subject to change, of the American Mineralogist (MSA)
Cite as Authors (Year) Title. American Mineralogist, in press.
(DOI will not work until issue is live.) DOI: http://dx.doi.org/10.2138/am.2013.4550

Revision 1

H-D interdiffusion in brucite at pressures up to 15 GPa

Xinzhuan Guo,* Takashi Yoshino, Takuo Okuchi, and Naotaka Tomioka

Institute for Study of the Earth's Interior, Okayama University, Misasa, Tottori 682-0193, Japan

*E-mail: gxzhuan@misasa.okayama-u.ac.jp

Abstract

Proton diffusion in brucite was investigated by conducting hydrogen (H)-deuterium (D) exchange experiments using multianvil high-pressure apparatuses at pressures from 3 to 15 GPa and temperatures in the range of 750-1050 K. Diffusion couple was composed of natural proton-dominated brucite single crystal surrounded by synthesized D-doped brucite polycrystals. Micro-Raman spectroscopy was used to determine the diffusion profiles of the samples. The D/H diffusion profile across the boundary between single crystal and polycrystalline D-doped brucite showed asymmetric pattern characterized by faster diffusion in aggregates. D/H interdiffusion rate determined from the analysis of single crystal side indicates that the interdiffusion rate increases with increasing H/D ratio. The H-D interdiffusion rate in the direction perpendicular to the *c*-axis is about 0.5 order of magnitude higher than that in the direction parallel to the *c*-axis. At 3 GPa, the H-D interdiffusion coefficients [D (m^2/s)] along and perpendicular to the *c*-axis of brucite at compositions of $C_{OD}^{Norm} = 0.2$ in the single crystal region were determined to be $3.30\ (177)\times10^{-11}\exp[-48.2(58)$ (KJ/mol)/RT] and $1.43\ (133)\times10^{-9}\exp[-67.5(232)$ (KJ/mol)/RT], respectively. H-D

interdiffusion rate perpendicular to and along the *c*-axis increased about one order of magnitude by compression from 3 to 10 GPa, but the pressure enhancement became weaker above 10 GPa. From 10 to 15 GPa, there is almost no pressure dependence of proton diffusion for both directions. As pressure increases up to 10 GPa, enhancement of the proton migration is strongly correlated with the activation of the atomic interaction and decrease of O…O' distance induced by compression. The positive pressure effect on the proton diffusion in brucite suggests that proton diffusion in higher-pressure hydrous phase becomes faster because of the shorter O…O' distance.

Keywords: brucite, H-D interdiffusion, diffusion, high pressure, Raman spectroscopy

Introduction

Diffusion of proton plays a key role in numerous behaviors in hydrous minerals such as plastic deformation, reaction kinetics and electrical conductivity. Diffusion of proton is closely related to the hydrogen bonding, interaction between atoms and the crystal structure of the hydrous minerals. Though uncommon in the deep Earth, brucite serves as a useful prototype for hydrous and layered minerals at high pressures (e.g., dense hydrous magnesium silicates), which are potential hosts for water and water-derived species in the mantle (Shieh et al., 1998; Ohtani et al., 2001). The crystal structure of brucite is in trigonal symmetry (Fig. 1), $P\bar{3}m1$, with $Mg(OH)_6$ octahedral layers stacking along the *c*-axis and the OH dipole orienting parallel to the *c*-axis on a three-fold axis (Bragg and Claringbull, 1965). Study of the proton

This is a preprint, the final version is subject to change, of the American Mineralogist (MSA)
Cite as Authors (Year) Title. American Mineralogist, in press.
(DOI will not work until issue is live.) DOI: http://dx.doi.org/10.2138/am.2013.4550

diffusion as simple hydroxide will provide insights into mechanisms of proton diffusion in other hydrous minerals relevant of the Earth's interior. Previous experimental studies revealed that the proton diffusivities in different hydrous minerals show large varieties (Marion et al., 2001; Noguchi and Shinoda, 2010; Graham et al., 1987), more than four orders in magnitude. It is important to compare the proton diffusivity in brucite with other hydrous minerals. It has been believed that the protons in $Mg(OH)_2$ occurs as only one migration mechanism, presumably as ground-level tunneling assisted by lattice phonons (Freund et al., 1975). Later, proton conductivity in $Mg(OH)_2$ powders reported by Freund and Wengeler (1980) indicated two kinds of conduction mechanisms: n-type (holes as charge carriers) and p-type (electrons as charge carriers). Recently, Noguchi and Shinoda (2010) favored the extrinsic vacancy mechanism for proton migration in portlandite [$Ca(OH)_2$], another isomorph of brucite, in the direction along the proton layer. Therefore, proton diffusivity data parallel and perpendicular to the *c*-axis are necessary to understand and quantify the different proton diffusion mechanisms as a function of the crystallographic direction.

Pressure effect on the arrangement of hydrogen in brucite is widely investigated by theoretical studies and various experimental techniques. The previous studies focused on whether brucite forms pressure-induced hydrogen bond between hydroxyls on a brucite layer and oxygen on the adjacent layer or not (Sherman, 1991; D'Arco et al., 1993; Parise et al., 1994; Catti et al., 1995). The study of Martens and Freund (1976) suggested that the potential barrier for proton transfer between two

This is a preprint, the final version is subject to change, of the American Mineralogist (MSA)
Cite as Authors (Year) Title. American Mineralogist, in press.
(DOI will not work until issue is live.) DOI: http://dx.doi.org/10.2138/am.2013.4550

neighboring hydrogen atoms in brucite would be reduced by compression. Infrared (IR) study of Shinoda and Aikawa (1998) and theoretical calibrations by Mookherjee and Stixrude (2006) have both shown that the proton transfer across interlayer might be strongly enhanced under pressure, that is, the pressure has a positive effect on the mobility of proton. Therefore, the pressure effect on the proton diffusion is still controversial. However, there are no experimental data about the proton diffusivity in brucite under high pressures to certify the pressure effect.

In this study we conducted a series of hydrogen-deuterium (H-D) interdiffusion experiments at various pressures and temperatures to assess the proton diffusion in brucite under high pressures and temperatures. Micro-Raman spectroscopy was used to determine the diffusion profile. Quantitative analyses of polymorphs using Raman spectroscopy have been attempted in previous studies (Kontoyannis and Vagenas, 2000; Fukuda et al., 2006), and have been successfully used in determining the proton diffusivity in portlandite (Noguchi et al., 2009; Noguchi and Shinoda, 2010). Based on this technique, we obtained diffusion profile and discussed the proton diffusion mechanism and its pressure effect.

Experimental methods

Sample preparation

Natural single crystal $Mg(OH)_2$ and synthesized $Mg(OD)_2$ powder were used as starting materials for a diffusion couple. For single crystal, the crystallographic orientation was determined by a precession X-ray camera, with a characteristic X-ray of Mo K_α. Microstructure observation by a field emission scanning electron

This is a preprint, the final version is subject to change, of the American Mineralogist (MSA)
Cite as Authors (Year) Title. American Mineralogist, in press.
(DOI will not work until issue is live.) DOI: http://dx.doi.org/10.2138/am.2013.4550

microscope (FE-SEM) indicated that the natural single crystal contained no inclusion of other minerals. As the cleavages are likely to develop along the (001) plane for brucite crystals, we carefully chose the sample without cracks under the optical microscope. The single crystal was cored to a cylindrical shape with 2 mm in diameter and 2 mm in length by ultrasonic drilling machine.

$Mg(OD)_2$ powder was synthesized from a mixture of MgO powder and D_2O with a ratio of 1:10 in weight using an autoclave and heated to a temperature up to 525 K and under autogenic pressure as high as 4 MPa for 168 hours. The synthesized sample was then baked in a vacuum stove at 473 K before the experiments to avoid contamination of H in air.

H-D exchange interdiffusion experiments

A series of H-D interdiffusion experiments was conducted using multi-anvil high-pressure apparatus. The diffusion experiments along the *c*-axis (the cylinder axis of diffusion couple is parallel to the *c*-axis of natural brucite single crystal) at 3 GPa were conducted using the DIA-type apparatus (Shimojuku et al., 2012). A cube of pyrophyllite with an edge length of 21 mm was used as a pressure medium. The diffusion experiments in the direction perpendicular to the *c*-axis at 3 GPa, and the other ones at higher pressures to 15 GPa, were conducted using a Kawai-type multi-anvil apparatus (Guo and Yoshino, 2013). Eight tungstencarbide anvils with truncation edge lengths of 15, and 6 mm were used to generate pressures up to 15 GPa. The cell assembly includes a pre-sintered Cr_2O_3-bearing MgO octahedral pressure medium, ZrO_2 thermal insulator and graphite cylindrical heater. The pressure

This is a preprint, the final version is subject to change, of the American Mineralogist (MSA)
Cite as Authors (Year) Title. American Mineralogist, in press.
(DOI will not work until issue is live.) DOI: http://dx.doi.org/10.2138/am.2013.4550

mediums have two edge lengths: 25 and 14 mm. Orientated and disk-shaped crystals of brucite were embedded in $Mg(OD)_2$ powder and welded in a Pt or Au capsule. An MgO insulating sleeve was placed between the graphite heater and the Pt (or Au) capsule. Temperature was monitored by a $WRe_{3\%}$-$WRe_{25\%}$ thermocouple. The detailed cell designs for the DIA-type and the Kawai-type apparatus are shown in Fig. 2.

For all experiments, pressure was firstly increased to desired value, and then heated up to designed temperatures within 3 minutes. The fast heating procedure is to minimize hydrogen diffusion below the target temperature. After annealed at the desired temperature, the sample was quenched within one minute to ambient temperature. Then recovered samples were confirmed to be brucite by micro-focused X-ray diffraction. The run products were mounted in epoxy and polished to the center of the cylindrical samples using silicon carbide papers without water to avoid hydrogen contamination. The recovered samples were polished in the direction perpendicular to the longitudinal section of cylindrical heater to obtain diffusion profiles. The surface roughness (about 5 μm), confirmed by a high resolution optical microscope, was distinctly smaller than the diffusion length (100-400 μm). The micro texture of the recovered diffusion couple was observed by FE-SEM (Fig. 3).

OD concentration calibration by Raman spectroscopy

To quantitatively estimate the concentration ratio of deuterium ($C_{OD} = \frac{100 \times C_{OD}}{C_{OD} + C_{OH}}\%$) over hydrogen ($C_{OH}$) in $Mg(OH)_2$-$Mg(OD)_2$ binary system by

This is a preprint, the final version is subject to change, of the American Mineralogist (MSA)
Cite as Authors (Year) Title. American Mineralogist, in press.
(DOI will not work until issue is live.) DOI: http://dx.doi.org/10.2138/am.2013.4550

micro-Raman spectroscopy, a standard curve was constructed using some brucite standards with various ratios (C_{OD}/C_{OH}). Four 'home made' standards with C_{OD} of 22%, 47%, 66% and 85% in each mole fraction were synthesized from mixtures of MgO powder, deuterated and protonated water. The deuterated and protonated water were weighed in designed ratios while keeping enough volumes to completely incorporate into the MgO powder. Every mixture was synthesized and evaluated by the same technique as used in synthesis of $Mg(OD)_2$ powder. Four standards were enclosed in four Au or Pt capsules with a diameter of 1 mm and a height of 2 mm separately and sintered simultaneously at 3 GPa and 1073 K for 2 h using a cubic anvil apparatus.

Raman spectroscopy measurements were performed using a micro-Raman spectrometer, which consists of Acton SpectraPro-300i monochromator with 300 mm in focal length, and a liquid-N_2 cooled charge-coupled device (CCD) detector. We used a grating with 1200 grooves per mm, which enabled us to simultaneously observe the OD and OH stretching vibrations. The wavelength was calibrated based on a numerical fit to the positions of the emission lines of neon gas. A green laser with 532 nm wavelength was used for exciting the Raman scattering in the range between 2384 and 3680 cm^{-1}. The laser beam was introduced into the Raman micro-spectrometer via an optical fiber, and it was focused on the surface of a sample through an objective lens (40×, N.A. 0.65) into the beam size of 2 μm in diameter. Duration of each point measurement was set between 30 to 180 s to provide adequate signal-to-noise ratio in the spectrum.

This is a preprint, the final version is subject to change, of the American Mineralogist (MSA)
Cite as Authors (Year) Title. American Mineralogist, in press.
(DOI will not work until issue is live.) DOI: http://dx.doi.org/10.2138/am.2013.4550

The measured intensity of the Raman scattering species *i* is represented as follows (Strommen and Nakamoto, 1984):

$$I_i(\nu) = I_0 K_i(\nu) C_i \quad (1)$$

where, I_0 is the incident intensity of the laser beam, v is the Raman frequency, C_i is the molar concentration per unit volume of species I, and $K(v)$ is a constant, including the frequency-dependent term, spectrometer response, self-absorption of the medium and scattering properties.

The relative intensity ratio of the Raman band of "OH" to "OD" is formulated as:

$$\frac{I_{OD}(v_{OD})}{I_{OH}(v_{OH}) + I_{OD}(v_{OD})} = \frac{C_{OD}}{C_{OD} + f(v_{OH}, v_{OD})(1 - C_{OD})} \quad (2)$$

where $f(v_{OH}, v_{OD}) = \frac{K'_{OH}(v_{OH})}{K'_{OD}(v_{OD})}$, C_{OD} is the mole fraction of "OH" in the mixture and $C_{OD} = 1 - C_{OH}$.

Then the calibration curve is derived from the transformation of equation (2):

$$C_{OD} = \frac{I_{OD}}{I_{OD} + f(v_{OH}, v_{OD})^{-1} I_{OH}} \quad (3)$$

C_{OD} is a fixed value and I_{OH} and I_{OD} can be measured by Raman spectroscopy for the four standards. The correlation factor between Raman intensity and C_{OD}, $f(v_{OH}, v_{OD})^{-1}$, was obtained by fitting the data acquired by equation (3).

Figure 4 shows representative Raman spectra for four standards with different C_{OD}. Peak-fitting analysis was performed by Gauss function with background correction using a horizontal base line. I_{OD} and I_{OH} were calculated based on their peak areas. I_{OD} increases with increasing C_{OD} in the sample. Raman spectra were

This is a preprint, the final version is subject to change, of the American Mineralogist (MSA)
Cite as Authors (Year) Title. American Mineralogist, in press.
(DOI will not work until issue is live.) DOI: http://dx.doi.org/10.2138/am.2013.4550

obtained from at least five different places of every standard, and most of the acquired data were consistent as shown in Fig. 5. By fitting the data points with the equation (3), we obtained the equation to calculate the C_{OD} as:

$$C_{OD} = \frac{I_{OD}}{I_{OD} + 1.28(5)\, I_{OH}} \quad (4)$$

Micro-Raman spectroscopy measurements for the run products of H-D interdiffusion experiments were acquired every 5 or 10 μm step. Representative Raman spectra of brucite parallel to the *c*-axis are shown in Fig. 6.

Calibration of the proton diffusivity in brucite

The observed diffusion profiles were asymmetric, which indicates that the diffusion rate is dependent on C_{OD}^{Norm}. We calculated the diffusion coefficient with the Boltzmann-Matano analysis using the equation:

$$D(C^*) = -\frac{1}{2t}\left(\frac{dx}{dC_{OD}^{Norm}}\right)_{C^*} \int_{C=0}^{C^*} x\, dC_{OD}^{Norm} \quad (5)$$

where $D(C^*)$ is the diffusion coefficient at the concentration C^*, t is the duration of the diffusion anneal, x is the position along the profile, and C_{OD}^{Norm} is normalized concentration.

The concentration $C_{OD}(x, t)$ at time t at a position x along the profile are normalized before treatment of the profiles by:

$$C_{OD}^{Norm} = \frac{C_{OD}(x,t) - C_r}{C_l - C_r} \quad (6)$$

with C_l and C_r denoting the initial concentrations of the two endmembers of the diffusion couples. The initial conditions at time $t = 0$ can be expressed in terms of the

This is a preprint, the final version is subject to change, of the American Mineralogist (MSA)
Cite as Authors (Year) Title. American Mineralogist, in press.
(DOI will not work until issue is live.) DOI: http://dx.doi.org/10.2138/am.2013.4550

normalized concentration. The zero point of the spatial coordinate x is defined by the Matano interface to satisfy the condition:

$$\int_{C_0}^{C_1} x \mathrm{d}C_{\mathrm{OD}}^{\mathrm{Norm}} = 0 \quad (7)$$

where C_0 and C_1 are the normalized starting compositions of the diffusion couple. We calculated the integral parts by counting squares $x\mathrm{d}C_{\mathrm{OD}}^{\mathrm{Norm}}$. The gradient $(\frac{\mathrm{d}x}{\mathrm{d}C_{\mathrm{OD}}^{\mathrm{Norm}}})_{C^*}$ was calculated from the tangent of the parabola which was obtained by curve-fitting to the original data points in the $Mg(OD)_2$ and $Mg(OH)_2$, respectively.

Results

The experimental conditions and results are summarized in Table 1. Figure 7 shows the H-D exchange diffusion profiles and the fitting results in different temperatures and pressures. Some diffusion profiles were remarkably asymmetric and significant changes of the slope were clearly observed in the diffusion profile at the interface, indicating that the diffusion rate changed discontinuously. Such a discontinuity is likely to imply the grain boundary diffusion effect in deuterated brucite aggregates. The maximum diffusion lengths in the direction perpendicular to or along the *c*-axis of the single crystal were both less than 400 μm. The sample dimension with 2 mm in diameter and 2 mm in height indicates that *D* values obtained from both directions of perpendicular to and along the *c*-axis were not influenced by the sample dimension. Zero time experiment at 3 GPa and 750 K shows that the diffusion length is less than 5 μm and the peak intensity is very weak, indicating the

This is a preprint, the final version is subject to change, of the American Mineralogist (MSA)
Cite as Authors (Year) Title. American Mineralogist, in press.
(DOI will not work until issue is live.) DOI: http://dx.doi.org/10.2138/am.2013.4550

hydrogen diffusion is negligible.

For some experiments, the intensity of Raman spectroscopy was weak at the interface of the diffusion couple and the noise was high, in which case we could not obtain the diffusion profile at C_{OD}^{Norm} in the range of 0.35-0.50 and 0.60-0.80. Therefore we estimated the diffusion coefficient for each side of the diffusion couple at C_{OD}^{Norm} = 0.9, 0.3 and 0.2 using the Boltzmann-Matano analysis. The H-D interdiffusion rate increases with increasing temperature at 3 GPa. The temperature dependence of diffusivity is given by:

$$D = D_0 \exp(\frac{-H}{RT}) \quad (8)$$

where D_0 is the pre-exponential factor, H is the activation enthalpy, R is the gas constant and T is the absolute temperature. The experimental reproducibility was checked by three experiments in the direction perpendicular to the *c*-axis at 3 GPa and 950 K with different duration: 1, 4 and 11 h. The deviation in log D is less than 5%. The deuterium diffusion distance in $Mg(OH)_2$ single crystals increased with increasing annealing time at same P/T conditions.

Figure 8 shows the temperature dependence of proton diffusion coefficient at 3 GPa. The location of the Matano interface, at which the C_{OD}^{Norm} is about 0.5-0.8, is on the $Mg(OD)_2$ side by about 5-10 μm relative to the original diffusion interface. The diffusion coefficient at C_{OD}^{Norm} = 0.2 is slightly larger than that at C_{OD}^{Norm} = 0.3, suggesting that the H-D interdiffusion rate is compositionally dependent. On the other hand, the diffusion rate at C_{OD}^{Norm} = 0.9 is about 0.5-1.5 times larger than that at C_{OD}^{Norm} = 0.2 and 0.3. The H-D interdiffusion rate in the direction perpendicular to the

237 *c*-axis of brucite is about a half order of magnitude higher than that in the direction
238 parallel to the *c*-axis. A least-squares fit of Eq. (8) to the diffusion data at C_{OD}^{Norm} = 0.2,
239 0.3 and 0.9 for the diffusion along the *c*-axis yields the pre-exponential factor (D_0) of
240 3.30 (±1.77)×10^{-11}, 3.95 (±1.73)×10^{-11} and 6.10 (±5.97)×10^{-9} m^2/s and activation
241 enthalpies (ΔH) of 48.2 (58), 50.2 (39) and 92.6 (212) KJ/mol, respectively. Arrhenius
242 parameters at C_{OD}^{Norm} = 0.2, 0.3 and 0.9 in the direction perpendicular to the *c*-axis
243 yield D_0 of 1.43 (133)×10^{-9}, 8.57 (822)×10^{-10} and 1.81 (178)×10^{-9} m^2/s and ΔH of
244 67.5 (232), 65.6 (222) and 56.0 (354) KJ/mol, respectively. The ΔH for H-D
245 interdiffusion in the brucite single crystal is consistent with 58.9 KJ/mol for proton
246 migration in portlandite single crystal (Noguchi and Shinoda, 2010).

247 Figure 9 shows the pressure effect on proton diffusivity in brucite. The proton
248 diffusion rates at C_{OD}^{Norm} = 0.2 and 0.3 in the directions both perpendicular to and
249 along the *c*-axis increase with pressures from 3 to 15 GPa at constant temperature of
250 950 K. However, the pressure dependence becomes weaker at higher pressures, and
251 constant above 10 GPa. The proton diffusion rate at C_{OD}^{Norm} = 0.9 is not consistent
252 with those at C_{OD}^{Norm} = 0.2 and 0.3. For example, interdiffusion rates in the directions
253 both perpendicular to and along the *c*-axis at C_{OD}^{Norm} = 0.9 at 3 GPa are much higher
254 than those at C_{OD}^{Norm} = 0.2 and 0.3, but they are comparable at higher pressures. This
255 inconsistency is likely to be originated from the grain boundary diffusion in D-brucite
256 aggregate. Because the degree of compaction of $Mg(OD)_2$ powder during preparing
257 the experimental cell is unavoidably different for each experiment. As a result, the
258 pressure effect on the grain boundary diffusion is likely to be very different run by run

This is a preprint, the final version is subject to change, of the American Mineralogist (MSA)
Cite as Authors (Year) Title. American Mineralogist, in press.
(DOI will not work until issue is live.) DOI: http://dx.doi.org/10.2138/am.2013.4550

(Sutton and Balluffi, 1995). The proton diffusion in the single crystal, on the contrary, is less influenced. Therefore, in the following discussion we focus on the interdiffuion rate at C_{OD}^{Norm} = 0.2 and 0.3 (in the single crystal side).

Discussion

H/D isotope effect on the Raman peak shift and the H-D interdiffusion rates

Figure 10 shows the frequencies of the O-H stretching vibration increases with C_{OD}^{Norm}, whereas O-D stretching exhibits a negative frequency shift. These peak shifts are likely caused by H/D isotope effect in the structural parameters of brucite. Neutron powder diffraction measurements of brucite (Chakoumakos et al., 2013) have shown that the O-H distances are longer than O-D distances. In a brucite single crystal, the average O-H length will be shortened if more H is substituted by D, and the O-D length will be lengthened if more D is substituted by H. As a result, the O-H bond will increase and O-D bond will decrease with increasing C_{OD}^{Norm}.

Chakoumakos et al.'s study (2013) showed that nearest-neighbor D…D distances in $Mg(OD)_2$ are longer than the H…H distances in $Mg(OH)_2$ due to the longer distance of O-H than that of O-D. Therefore, if more H in $Mg(OH)_2$ was replaced by D during H-D interdiffusion experiment, the average H…H distances would increase, that is, the H diffusion became difficult due to the larger jumping distance. Our H-D interdiffusion experiments showed that the H-D interdiffusion rates at C_{OD}^{Norm} = 0.3 were lower than that at C_{OD}^{Norm} = 0.2 (Fig. 8) is likely due to this H/D isotope effect in brucite.

Proton diffusion mechanism

This is a preprint, the final version is subject to change, of the American Mineralogist (MSA)
Cite as Authors (Year) Title. American Mineralogist, in press.
(DOI will not work until issue is live.) DOI: http://dx.doi.org/10.2138/am.2013.4550

The hydroxyl protons in $Mg(OH)_2$ are tightly bound to the O^{2-} ions, because the O-H distance for brucite (less than 0.958 Å: Catti et al., 1995) is shorter than the ionic radius of O^{2-} ions (1.33-1.40 Å: Freund and Wengeler, 1980). To escape from the hydroxyl lattice, protons must in some way become mobile via:

$$OH^- + OH^- \Leftrightarrow HOH + O^{2-} \quad (9)$$

where HOH is considered as the excess proton on a lattice site. O^{2-} denotes a vacancy in the H site. The excess proton will have a certain probability to diffuse away through the lattice and becomes an excess proton in the hydroxide lattice according to:

$$HOH + OH^- \Leftrightarrow OH^- + HOH \quad (10)$$

The excess proton may move through the lattice using interstitial sites. On the other hand, the O^{2-} can enter a hydrogen-bond type interaction with one of the three neighboring OH^- leading to a proton exchange:

$$O^{2-} + OH^- \Leftrightarrow OH^- + O^{2-} \quad (11)$$

Reaction (10), an interstitial mechanism, controls the proton migration along the *c*-axis of brucite. In this mechanism, an interstitial proton can diffuse by jumping from one interstitial site to one of its neighboring sites. This mechanism is unlikely to appear for the proton diffusion perpendicular to the *c*-axis of brucite, because there are no possible equilibrium positions for an interstitial proton to settle due to the proton-proton repulsive interaction in the proton layer. Reaction (11), a vacancy mechanism, is a dominant mechanism for proton migration perpendicular to the *c*-axis. Proton in a normal lattice position can jump into a neighboring vacancy. The total

This is a preprint, the final version is subject to change, of the American Mineralogist (MSA)
Cite as Authors (Year) Title. American Mineralogist, in press.
(DOI will not work until issue is live.) DOI: http://dx.doi.org/10.2138/am.2013.4550

vacancies in H sites include ones generated by thermally activated process (reaction (9), intrinsic mechanism) and ones introduced to compensate the charge balance due to the chemical impurities (in the order of 10^{-3} for the starting materials in our experiments) in the structure via extrinsic mechanism. We can estimate the intrinsic defects concentration (including excess protons and vacancies in H sites) by the following equation (Chiang et al., 1997):

$$\frac{n}{N} = \exp(-\frac{\Delta G}{2RT}) = \exp(\frac{\Delta S}{2R})\exp(-\frac{\Delta H}{2RT}) \quad (12)$$

where n is the intrinsic defects, N is ideal lattice sites, ΔG is the formation Gibbs energy (KJ/mol), ΔS is nonconfiguration entropy, ΔH is the formation energy (KJ/mol). Usually, $\exp(\frac{\Delta S}{2R})$ ~1 and ΔH = 144.7 KJ/mol. The intrinsic defect concentration is estimated to be 9.12×10^{-6} to 2.51×10^{-4} in the temperature range of 750-1050 K. Therefore, the total amount of vacancy is higher than that of interstitial proton. Our results demonstrated that the proton diffusion perpendicular to the *c*-axis is faster (0.5 order of magnitude higher) than that along the *c*-axis. The diffusion anisotropy can be explained by different diffusion mechanisms in the directions perpendicular to and along the *c*-axis of brucite. The lower activation enthalpy for proton diffusion along the *c*-axis indicates that the lower potential barrier for interstitial proton to migrate from one equilibrium position to the neighboring sites.

Pressure effect on the proton diffusivity in brucite

The enhancement of proton migration perpendicular to the *c*-axis of brucite at high pressure is closely related to the structural change of brucite as pressure

This is a preprint, the final version is subject to change, of the American Mineralogist (MSA)
Cite as Authors (Year) Title. American Mineralogist, in press.
(DOI will not work until issue is live.) DOI: http://dx.doi.org/10.2138/am.2013.4550

325 increases. Neutron diffraction studies at pressures up to 11 GPa (Parise et al., 1994;
326 Catti et al., 1995) indicated that H atom disordered off the threefold axis by
327 compression. In the disordered structure H approaches one of the three neighboring
328 O' atoms, and geometrical conditions much more favorable for hydrogen bonding are
329 set up: the H…O' distance diminishes and the <OHO' angle widens substantially.
330 Interlayer compression shortens the O…O' distance (between donors OH and the
331 acceptors O' in the neighboring layer), and simultaneously increases the strength of
332 the bonding between H and O atoms in the next layer. The potential barrier between
333 proton sites in adjacent OH^- groups is proportional to the O…O' distance (Martens
334 and Freund, 1976). Therefore the proton migration through equation (11) is enhanced
335 by compression. Pressure effect on the proton transfer was also confirmed by the
336 infrared (IR) spectroscopy study. Shinoda and Aikawa (1998) reported the
337 pressure-induced IR absorption peak at 3645 cm^{-1} above 2.9 GPa at room temperature,
338 and proposed the formation of a new OH dipole in brucite at high pressures. The
339 formation processes of the new OH dipole and its reverse pleochroism can be
340 considered as proton transfer between brucite layers at higher pressures. The IR
341 synchrotron radiation study of brucite at high pressure and temperature (Shinoda et al.,
342 2002) showed that the pressure-induced peak above 3 GPa at room temperature
343 disappeared at higher temperature (above 493 K), whereas a broad absorption band
344 was observed, suggesting a possibility of proton conduction in brucite at higher
345 pressures and temperatures. Our diffusion experiments showed that the hydrogen
346 diffusion perpendicular to the *c*-axis is strongly enhanced from 3 to 10 GPa, which

This is a preprint, the final version is subject to change, of the American Mineralogist (MSA)
Cite as Authors (Year) Title. American Mineralogist, in press.
(DOI will not work until issue is live.) DOI: http://dx.doi.org/10.2138/am.2013.4550

can be explained by the strengthened proton transfer induced by shortening jumping distance and lowered potential barrier during compression. The enhancement of proton diffusion, however, becomes weaker on further compression from 10 GPa. This change can be explained by the completion of rearrangements of the H atoms and a change of the compression mechanism upon further compression. Upon compression, the H…O' interaction characterized by an attractive force will be balanced by the increasing H…H' repulsive force, thus at certain pressure (around 10 GPa) the disordered structure becomes energetically stable. X-ray diffraction (Fei and Mao, 1993; Duffy et al., 1995; Nagai et al., 2000; Ma et al., 2013) and neutron diffraction (Parise et al., 1994; Catti, et al., 1995) showed that there is a rapid decrease in the pressure dependence of *c*/*a* at around 10 GPa, above which the compression behavior of brucite becomes isotropic. The study of Nagai et al. (2000) suggested that the shortening of the interlayer distance controls compression below 10 GPa, whereas above this pressure compression of the [MgO_6] octahedral becomes the dominant mechanism. The potential barrier between proton sites in adjacent layers will no longer change significantly after brucite is compressed to 10 GPa. Therefore, proton diffusivity becomes pressure independent above 10 GPa.

The change of O…O' distance upon compression and the resultant changes of structure and compression mechanism control the proton diffusion perpendicular to the *c*-axis of brucite. The proton diffusion along the *c*-axis of brucite also can be explained by the changes of O…O' distance. Upon compression from 3 to 10 GPa, the O…O' distance largely decreases and the jumping distance between interstitial

This is a preprint, the final version is subject to change, of the American Mineralogist (MSA)
Cite as Authors (Year) Title. American Mineralogist, in press.
(DOI will not work until issue is live.) DOI: http://dx.doi.org/10.2138/am.2013.4550

proton and the neighboring sites also decreases significantly. Above 10 GPa, the compressibility of the crystal along the *c*-axis becomes smaller. Proton diffusion, therefore, becomes relatively less pressure independent.

Pressure effect on the proton diffusivity in brucite would shed light on the explanation on a variation of electrical conductivity of dense hydrous magnesium silicate (DHMS) phases. For example, phase D (higher pressure phase of DHMS) has much higher electrical conductivity than phase A and super-hydrous phase B (Guo and Yoshino, 2013). Given that the vacancy mechanism is dominant in those minerals, the total number of vacancies should be within one order at the same temperature range. In this case, the proton diffusion in phase D is the fastest based on Nernst-Einstein equation. Considering that the shortest O…O' distance of phase D, we can conclude that pressure effect on the O…O' distance is an important controlling parameter for the electrical conductivity of phase D.

Comparison with other hydrous minerals

Figure 11 compares the proton diffusion rates of brucite with those of other hydrous minerals. Hydrogen diffusivities in brucite, portlandite and epidote are comparable but are much higher in the same temperature range than those of muscovite, zoisite, chlorite and lawsonite and the activation enthalpies of brucite, portlandite and epidote are 0.70, 0.61 and 0.60 eV, respectively. In general, hydrous minerals showing lower H diffusivities have higher activation enthalpy more than 1 eV. For example, hydrogen diffusion in chlorite is slowest (about 2-4 orders of magnitude lower than that in brucite) with higher activation enthalpy of 1.78 eV.

This is a preprint, the final version is subject to change, of the American Mineralogist (MSA)
Cite as Authors (Year) Title. American Mineralogist, in press.
(DOI will not work until issue is live.) DOI: http://dx.doi.org/10.2138/am.2013.4550

Despite the structural similarity of epidote and zoisite, hydrogen diffusivities in zoisite are about 1.5 orders of magnitude lower than that in epidote. Hydrogen diffusivity in muscovite is comparable with that in chlorite, but the activation enthalpy (1.25 eV) is much lower than that for chlorite.

Graham (1981) proposed that the transport of hydrogen in epidote and zoisite is proceeded by hydrolysis of the Si-O and Al-O bonds, followed by proton transfer by a slower diffusion of (OH) or H_2O. OH or H_2O species are unlikely to diffuse in hydrous minerals, especially at low temperature, because of the strong bonding of Si-O, Al-O and Mg-O. Proton jumping alone between relatively stationary oxygen ions, so-called Grotthus mechanism (Marion et al., 2001), should control the proton diffusion in nominally hydrous minerals. As discussed above, proton diffusion in a crystal seems to be strongly controlled by the relevant interaction between the neighboring hydroxyls. The faster proton diffusion in brucite and portlandite is caused by only the shorter distance between the proton sites compared with other hydrous minerals.

Because brucite and portlandite are the isomorphs with the same simplest structure, the proton diffusivities in these two minerals are much more comparable. The slightly faster proton diffusion in brucite than that in portlandite in the direction perpendicular to the *c*-axis (Noguchi and Shinoda, 2010) might be due to the higher experimental pressure for brucite. Our experiments show that pressure can greatly enhance the proton transfer below 10 GPa. Though brucite and portlandite exhibit some different behaviors at high pressure, e.g., portlandite undergoes a

This is a preprint, the final version is subject to change, of the American Mineralogist (MSA)
Cite as Authors (Year) Title. American Mineralogist, in press.
(DOI will not work until issue is live.) DOI: http://dx.doi.org/10.2138/am.2013.4550

pressure-induced amorphization between 10.7 and 15.4 GPa (Kruger et al., 1989; Meade and Jeanloz, 1990) and brucite does not, they exhibit similar behaviors before 5 GPa. Upon compression H becomes even more disordered in portlandite, resulting in strengthened H bonding between the two neighboring [CaO_6] layers compared with that in brucite. Therefore, we predict that the proton diffusion in portlandite is faster than that in brucite under the same pressure, e.g., 3 GPa.

Concluding remarks:

H-D interdiffusion rates in brucite at pressures up to 15 GPa were investigated. Line analysis of micro-Raman spectroscopy measurement was performed to obtain the H/D diffusion profile across the boundary between H- and D-doped brucite. OH/OD peak intensity ratio for binary system of $Mg(OH)_2$ and $Mg(OD)_2$ was determined from Raman spectra of brucite aggregates with various H/D ratios and its correlation factor was 1.28.

The diffusion profiles across the boundary between D-doped brucite aggregates and H brucite single crystal were asymmetric due to contribution of the grain boundary diffusion to the bulk diffusion in the polycrystal side. The H-D interdiffusion rates were compositionally dependent. In the single crystal side, the proton diffusivity decreases with increasing C_{OD}^{norm}. Proton diffusion along the [MgO_6] octahedral layer is about a half order of magnitude higher than that perpendicular to the [MgO_6] octahedral layer. The H-D interdiffusion rates increase with temperature. The relationship between proton diffusivity and reciprocal temperature can be

435 expressed by Arrhenian formula. The activation enthalpy (0.5-0.7 eV) for proton
436 diffusion in $Mg(OH)_2$ single crystal is consistent with that (0.61 eV) in portlandite
437 single crystal.

438 Vacancy mechanism is a dominant one for proton diffusion along the $[MgO_6]$
439 octahedral layer, in which case hydrogen can jump to the neighboring hydrogen
440 vacancy through a hydrogen-bond type interaction [reaction (11)]. Interstitial
441 mechanism also can enhance proton diffusion perpendicular to the *c*-axis through
442 reaction (10).

443 Although atomic motion is generally decreased with increasing pressure, the
444 proton in brucite migrates more actively due to the activation of the atomic interaction.
445 O…O' distance is an important parameter for proton diffusion in brucite, which is
446 strongly correlated with the interaction between hydroxyls on a brucite layer and
447 oxygen on the adjacent layer. The positive pressure effect on the proton diffusion in
448 brucite suggests that proton diffusion in higher-pressure hydrous phase becomes faster
449 because of the shorter O…O' distance.

450 **Acknowledgements**

451 We acknowledge D. Yamazaki, A. Yoneda, and E. Ito for their helpful
452 suggestions and comments. This study was supported by a Grant-in-Aid for Scientific
453 Research in Innovative Areas (Research in a Proposed Research Area), "Geofluids:
454 Nature and Dynamics of Fluids in Subduction Zones" from the Japan Society for
455 Promotion of Science (No. 2109003).

456

457 **References:**

458 Bragg, W.L. and Claringbull, G.F. (1965) Crystal structure of minerals, 409 p. Bell,
459 London.

460 Catti, M., Ferraris, G., Hull, S., and Pavese, A. (1995) Static compression and H
461 disorder in brucite, $Mg(OH)_2$, to 11 GPa: a powder Neutron diffraction study.
462 Physics and Chemistry of Minerals, 22, 200-206.

463 Chakoumakos, B. C., Horita, J., and Garlea, V.O. (2013) H/D isotope effects in
464 brucite at low temperatures. Amercan Mineralogist, 98, 1-6.

465 Chiang, Y.M., Birnie, D.P., and Kingery, W.D. (1997) Physical Ceramics: Principles
466 for Ceramic Science and Engineering, 532 p. Wiley, New York.

467 D'Arco, Ph, Causa, M. and Silvi, B. (1993) Periodic Hartree-Fock study of a weakly
468 bonded layer structure: brucite $Mg(OH)_2$. Physical Review B, 47, 3522-3529.

469 Fei, Y. and Mao, H. (1993) Static compression of $Mg(OH)_2$ to 78 GPa at high
470 temperature and constraints on the equation of state of fluid H_2O. Journal of
471 Geophysical Research, 98, 11875-11884.

472 Freund, F., Gieseke, W., and Nagerl, H. (1975) in: Reaction kinetics in heterogeneous
473 chemical systems, 2nd ed., 804 p. Elesvier Publication, Amsterdam.

474 Freund, F. and Wengeler, H. (1980) Proton conductivity of simple ionic hydroxides.
475 Part I: the proton conductivities of $Al(OH)_3$, $Ca(OH)_2$ and $Mg(OH)_2$. Berichte
476 der Bunsengesellschaft fur Physikalische Chemie, 84, 866-873.

477 Fukuda, K., Ohotani, W., Matumoto, E., Kawashima, N., and Takata, T. (2006).
478 Novel analysis of inorganic-organic composites using Raman microscopy.

Journal of the Ceramic Society of Japan, 114, 782-786.

Graham, C.M. (1981) Experimental hydrogen isotope studies □: Diffusion of hydrogen in hydrous minerals, and stable isotope exchange in metamorphic rocks. Contributions to Mineralogy and Petrology. 76, 216-228.

Graham, C.M., Viglino, J.A., and Harmon, R.S. (1987) Experimental study of hydrogen-isotope exchange between aluminous chlorite and water and hydrogen diffusion in chlorite. American Mineralogist, 72, 566-579.

Guo, X. and Yoshino, T. (2013) Electrical conductivity of dense hydrous magnesium silicates with implication for conductivity in the stagant slab. Earth and Planetary Science Letters, http://dx.doi.org/10.1016/j.epsl.2013.03.026.

Duffy, T.S., Meade, C., Fei, Y., Mao, H.K. and Hemley, R.J. (1995) High-pressure phase transition in brucite, $Mg(OH)_2$. American Mineralogist, 80, 222-230.

Kontoyannis, C. and Vagenas, N. (2000). Calcium carbonate phase analysis using XRD and FT-Raman spectroscopy. Analyst, 125, 251-255.

Kruger, M.B., Williams, Q. and Jeanloz, R. (1989) Vibrational spectra of Mg(OH)2 and Ca(OH)2 under pressure. Journal of Chemical Physics, 91, 5910-5915.

Ma, M., Liu, W., Chen, Z., Liu, Z. and Li, B. (2013) Compression and structure of brucite to 31 GPa from synchrotron X-ray diffraction and infrared spectroscopy studies. American Mineralogist, 98, 33-40.

Meade, C. and Jeanloz, R. (1990) Static compression of $Ca(OH)_2$ at room temperature: observations of amorphization and equation of state measurements to 10.7 GPa. Geophysical Research Letters, 17, 1157-1160.

Marion, S., Meyer, H.W., Carpenter, M., and Norby, T. (2001) H_2O-D_2O exchange in lawsonite. American Mineralogist, 86, 1166-1169.

Marten, R. and Freund, F. (1976) The potential energy curve of the proton and dissociation energy of the OH^{-1} ion in $Mg(OH)_2$. Physical Status Solidi A, 37, 97-104.

Mookherjee, M. and Stixrude, L. (2006) High-pressure proton disorder in brucite. American Mineralogist, 91, 127-134.

Nagai, T., Hattori, T. and Yamanaka, T. (2000) Compression mechanism of brucite: An investigation by structural refinement under pressure. American Mineralogist, 85, 760-764.

Noguchi, N. and Shinoda, K. (2010) Proton migration in portlandite inferred from activation energy of self-diffusion and potential energy curve of OH bond. Physics and Chemistry of Minerals, 37, 361-370.

Noguchi, N., Shinoda, K., and Masuda, K. (2009) Quantitative analysis of binary mineral mixtures musing Raman microspectroscopy: calibration curves for silica and calcium carbonate minerals and application to an opaline silica nodule of volcanic origin. Journal of mineralogical and petrological sciences, 104, 253-262.

Ohtani, E., Toma, M., Litasov, K., Kubo, T., and Suzuki, A. (2001) Stability of dense hydrous magnesium silicate phases and water storage capacity in the transition zone and lower mantle. Physics of the Earth and Planetary Interiors, 124, 105-117.

Parise, J., Leinenweber, K., Weidner, D., and Tan, K. (1994) Pressure-induced H bonding: Neutron diffraction study of brucite, $Mg(OD)_2$ to 9.3 GPa. American Mineralogist, 79, 193-196.

Sherman, D.M. (1991) Hartree-Fock band structure, equation of state, and pressure-induced hydrogen bonding in brucite, $Mg(OH)_2$. American Mineralogist, 76, 1769-1772.

Shieh, S.R., Mao, H., Hemley, R.J., and Ming, L.C. (1998) Decomposition of phase D in the lower mantle and the fate of dense hydrous silicates in subducting slabs. Earth and Planetary Science Letters, 159, 13-23.

Shimojuku, A., Yoshino, T., Yamazaki, D., and Okudaira, T. (2012) Electrical conductivity of fluid-bearing quartzite under lower crustal conditions. Physics of the Earth and Planetary Interiors, 198-199, 1-8.

Shinoda, K. and Aikawa, N. (1998) Interlayer proton transfer in brucite under pressure by polarized IR spectroscopy to 5.3 GPa. Physics and Chemistry of Minerals, 25, 197-202.

Shinoda, K., Yamakata, M., Nanba, T., Kimura, H., Moriwaki, T., Kondo, Y., Kawamoto, T., Niimi, N., Miyoshi, N. and Aikawa, N. (2002) High-pressure phase transition and behavior of protons in brucite $Mg(OH)_2$: a high-pressure-temperature study using IR synchrotron radiation. Physics and Chemistry of Minerals, 29, 396-402.

Strommen, D. and Nakamoto, K. (1984) Laboratory Raman Spectroscopy, 146 p. Wiley, New York.

Sutton, A.P., Balluffi, R.W. (1995) Interfaces in Crystalline Materials. Clarendon Press, Oxford.

Clarendon Press, Oxford. Suzuoki, T. and Epstein, S. (1976) Hydrogen isotope fraction between OH-bearing minerals and water. Geochim Cosmochim Acta, 40, 1229-1240.

This is a preprint, the final version is subject to change, of the American Mineralogist (MSA)
Cite as Authors (Year) Title. American Mineralogist, in press.
(DOI will not work until issue is live.) DOI: http://dx.doi.org/10.2138/am.2013.4550

Figure captions

FIGURE 1. Crystal structure of brucite, $Mg(OH)_2$. (a) Side view of the brucite structure. Octahedra represent [MgO_6] units, dark grey balls are oxygen atoms, light grey balls denote hydrogen atoms. Note that each H atom is disordered over three positions about the threefold rotation with occupancy of 1/3. (b) Perspective view of the $P\bar{3}m1$ structure showing the downward pointing proton surrounded by three upward pointing protons. The Mg atoms are denoted by white balls, the oxygen atom by dark grey balls and the proton in the 2d position (1/3, 2/3, z_H) by light grey balls. The arrows denote the H…H interaction and point-dipole interaction.

FIGURE 2. Schematic cross-section of the cell assembly for H-D interdiffusion experiments at 3 GPa using a DIA-type apparatus (a) and a Kawai-type apparatus (b). Note that for the H-D exchange experiments at 10 and 15 GPa, an octahedral cell with edge length of 14 was used and a TiB_2-doped BN heater was used instead of the graphite heater.

FIGURE 3. Texture of diffusion couple (//*c*-axis) at 15 GPa and 950 K observed by FE-SEM. Boundary between $Mg(OH)_2$ single crystal and $Mg(OD)_2$ aggregates can be identified.

FIGURE 4. Representative Raman spectra of four standards with different C_{OD}. Peaks at 2696 and 3646 cm^{-1} were assigned to OD and OH stretching vibrations,

This is a preprint, the final version is subject to change, of the American Mineralogist (MSA)
Cite as Authors (Year) Title. American Mineralogist, in press.
(DOI will not work until issue is live.) DOI: http://dx.doi.org/10.2138/am.2013.4550

589 respectively.

590

591 **FIGURE 5.** Correlation between C_{OD} and $I_{OD}/(I_{OD}+I_{OH})$ for various $Mg(OH)_2$/
592 $Mg(OD)_2$ mixtures. The error of $I_{OD}/(I_{OD}+I_{CD})$, estimated from the calibration of area
593 of peak, is within the symbol. The red line shows the calibration curve for converting
594 I_{OD} and I_{OH} into C_{OD} (fit by Eq. 3). $C_{OD} = \frac{I_{OD}}{I_{OD} + 1.28(5)\, I_{OH}}$.

595

596 **FIGURE 6.** (a) An optical transmitted light microscopic image of a thin section along
597 the *c*-axis of brucite after H-D exchange experiment at 950 K and 3 GPa for 6.3 h.
598 The arrow indicates direction along which the Raman spectra were acquired. An
599 origin (0 μm) indicates the present boundary between $Mg(OH)_2$ single crystal and
600 polycrystalline $Mg(OD)_2$. (b) Sequential spectra measured at intervals of 5 μm along
601 the direction shown in (a) by a micro Raman spectrometer. Peaks at 2696 and 3646
602 cm^{-1} are assigned to OD and OH stretching vibrations, respectively. Some narrow
603 peaks were from the effect of cosmic waves.

604

605 **FIGURE 7.** (a-m) The profiles of the molar ratio of deuterium to hydrogen (C_{OD}^{norm}
606 profile) perpendicular to and along the *c*-axis of brucite at different P/T conditions.
607 The parabola obtained by curve-fitting to the raw data points, which was used to
608 calculate the gradient in Eq. (5), are also shown by the solid curves. Matano interfaces
609 are denoted by dashed lines. NC and PC denote perpendicular to and along the *c*-axis,

610 respectively.

611

612 **FIGURE 8.** H-D interdiffusion coefficients in brucite single crystal in the direction
613 along (a) and perpendicular to (b) the *c*-axis are plotted against reciprocal temperature.
614 Filled blue triangle, filled black squares and open red circles denote the diffusion data
615 at C_{OD}^{norm} = 0.9, 0.3 and 0.2, respectively. The blue, black and red lines represent the
616 fitting results at C_{OD}^{norm} = 0.9, 0.3 and 0.2, respectively. The errors in temperature were
617 estimated by temperature gradient in the cell (around ±10 K within 1 mm). The errors
618 of interdiffusion coefficients were estimated by the curve-fitting error from the raw
619 data.

620

621 **FIGURE 9.** H-D interdiffusion coefficients perpendicular to and along the *c*-axis of
622 brucite are plotted as a function of pressure. The open and filled black circles denote
623 the diffusion data perpendicular to the *c*-axis of brucite at C_{OD}^{norm} = 0.2 and 0.3,
624 respectively. The open and filled black squares denote the diffusion coefficients along
625 the *c*-axis of brucite at C_{OD}^{norm} = 0.2 and 0.3, respectively. The solid and dash line are
626 the non-linear fitting of the diffusion data perpendicular to and along the *c*-axis of
627 brucite at C_{OD}^{norm} = 0.2 by an asymptotic model.

628

629 **FIGURE 10.** O-H (a) and O-D (b) stretching vibration frequencies shift with C_{OD}.
630 The data are from the recovered sample for H-D interdiffusion along the *c*-axis at 15
631 GPa and 950 K. The data from all the recovered samples show the same dependence

This is a preprint, the final version is subject to change, of the American Mineralogist (MSA)
Cite as Authors (Year) Title. American Mineralogist, in press.
(DOI will not work until issue is live.) DOI: http://dx.doi.org/10.2138/am.2013.4550

of O-H and O-D stretching vibration frequencies on C_{OD}. The error in the measurement of frequency is within the size of the symbol.

FIGURE 11. Arrhenius plots of log *D* perpendicular to and along the *c*-axis of brucite and of the other hydrous minerals. The labeled numbers denote the OD concentration. The red and blue symbols represent the raw data obtained from this study, which are fitted by the least-squares method. Data for portlandite, lawsonite and chlorite are from Noguchi and Shinoda (2010), Marion et al. (2001) and Graham et al. (1987), respectively. Diffusion data for zoisite and epidote are from Graham (1981). Data for muscovite are calculated from Suzuoki and Epstein (1976).

This is a preprint, the final version is subject to change, of the American Mineralogist (MSA)
Cite as Authors (Year) Title. American Mineralogist, in press.
(DOI will not work until issue is live.) DOI: http://dx.doi.org/10.2138/am.2013.4550

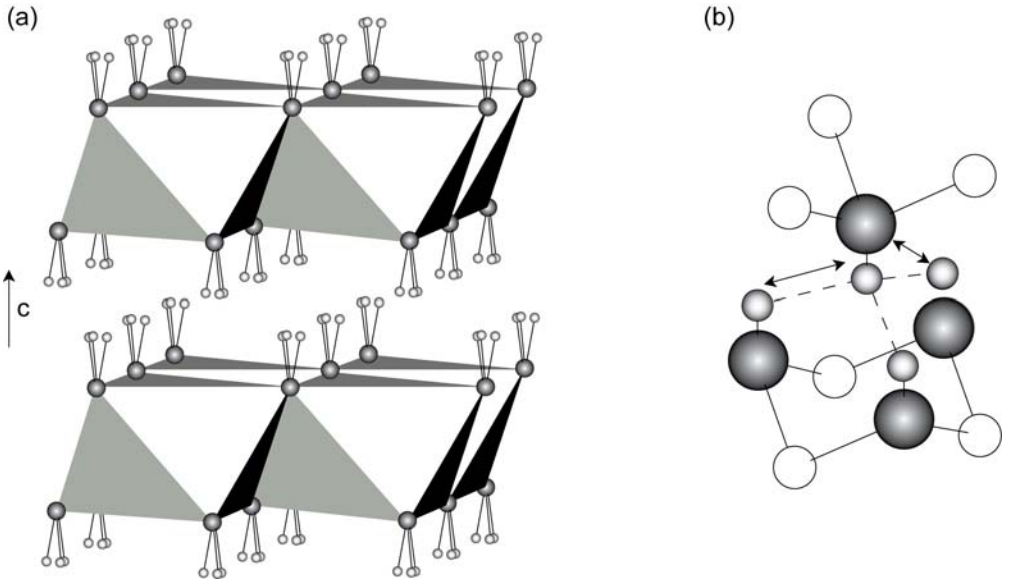

Figure 1. Guo et al.

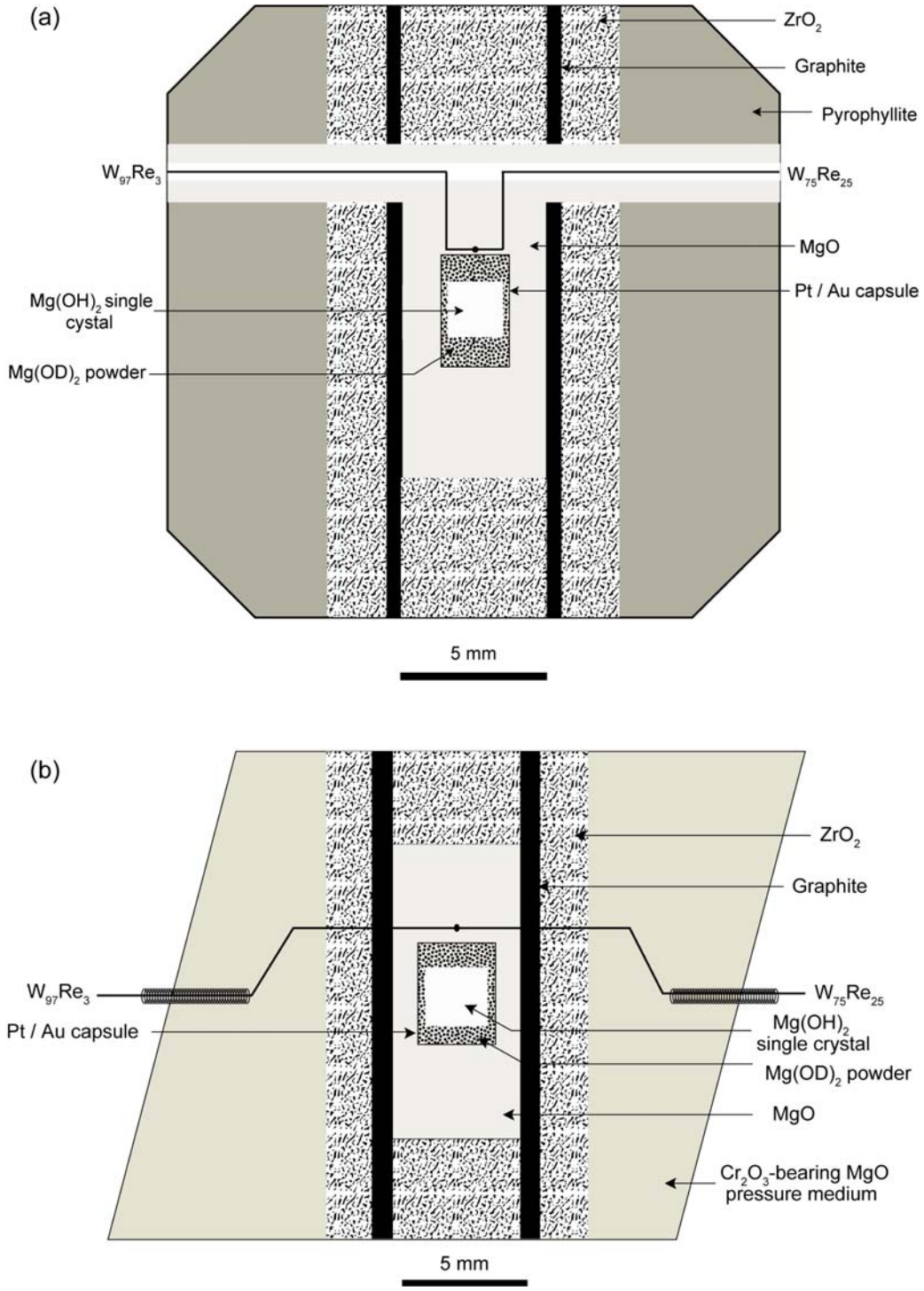

669

670 Figure 2. Guo et al.

671

This is a preprint, the final version is subject to change, of the American Mineralogist (MSA)
Cite as Authors (Year) Title. American Mineralogist, in press.
(DOI will not work until issue is live.) DOI: http://dx.doi.org/10.2138/am.2013.4550

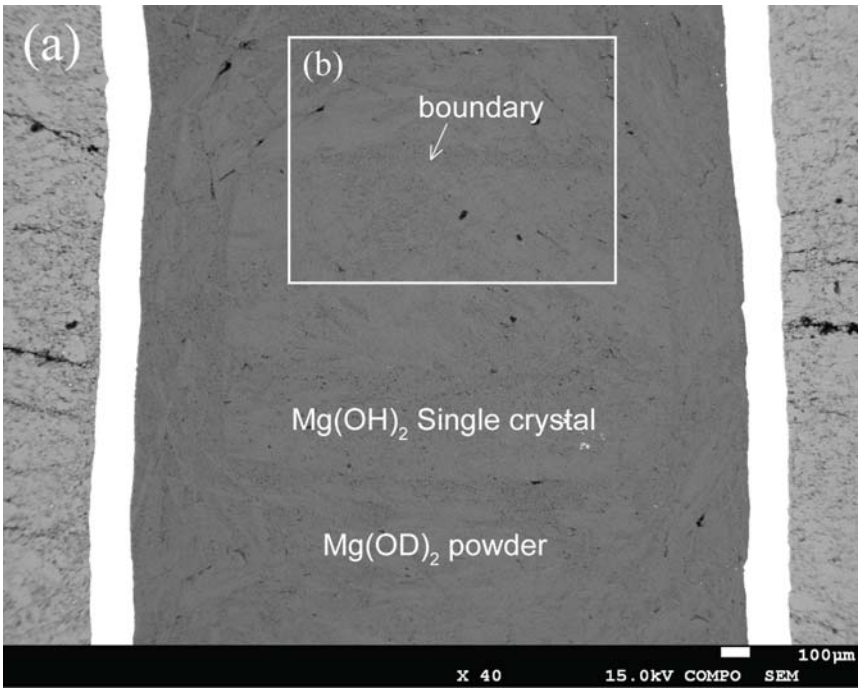

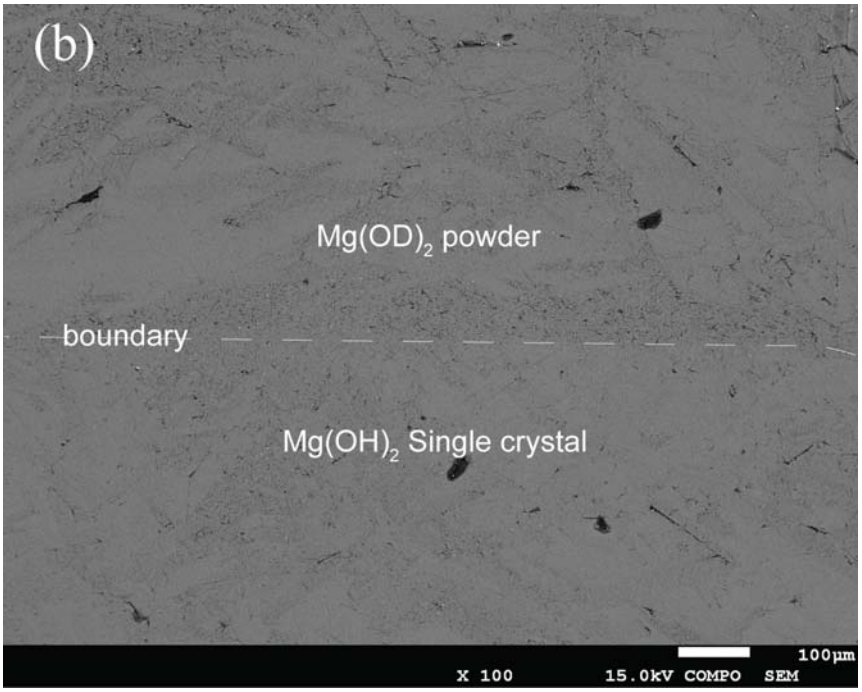

Figure 3. Guo et al.

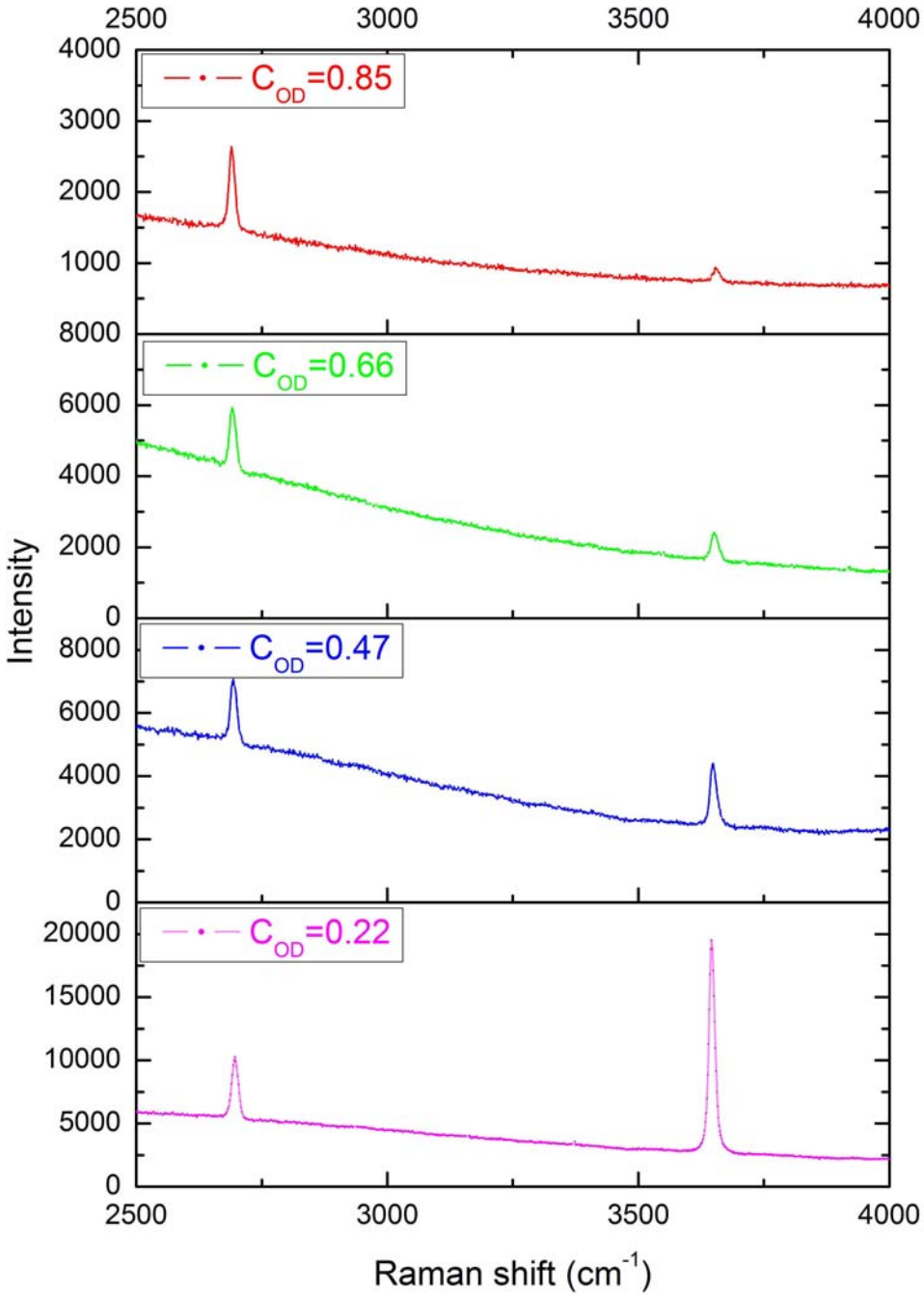

Figure 4. Guo et al.

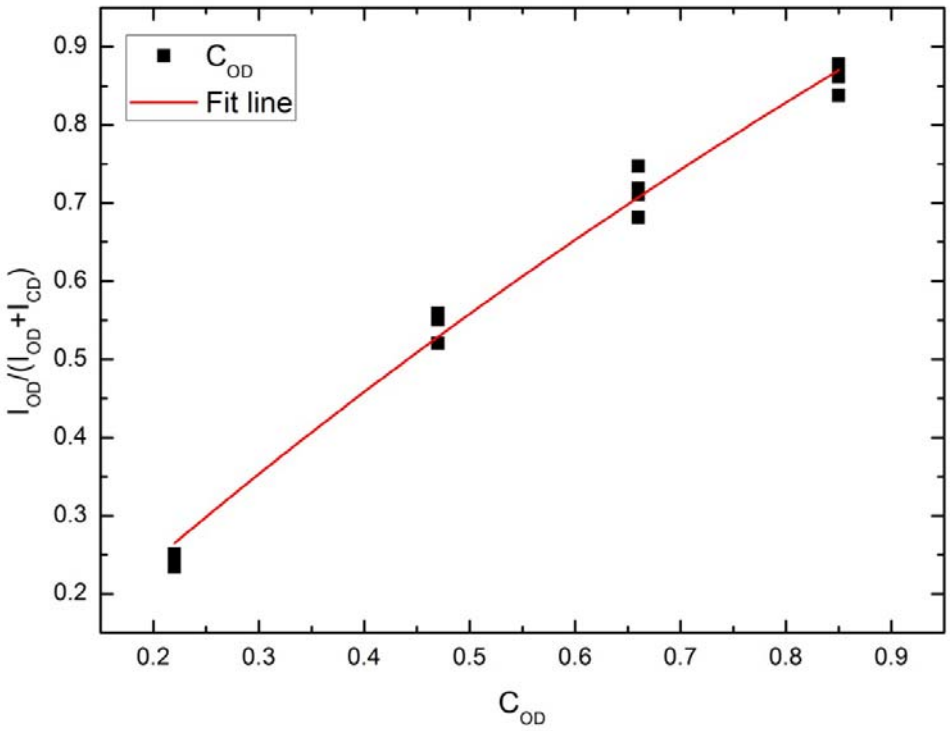

Figure 5. Guo et al.

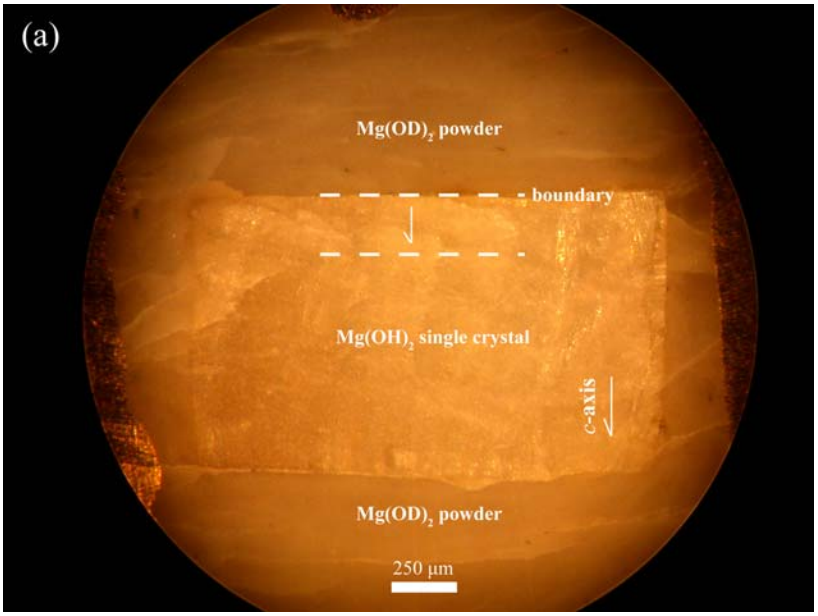

(b)

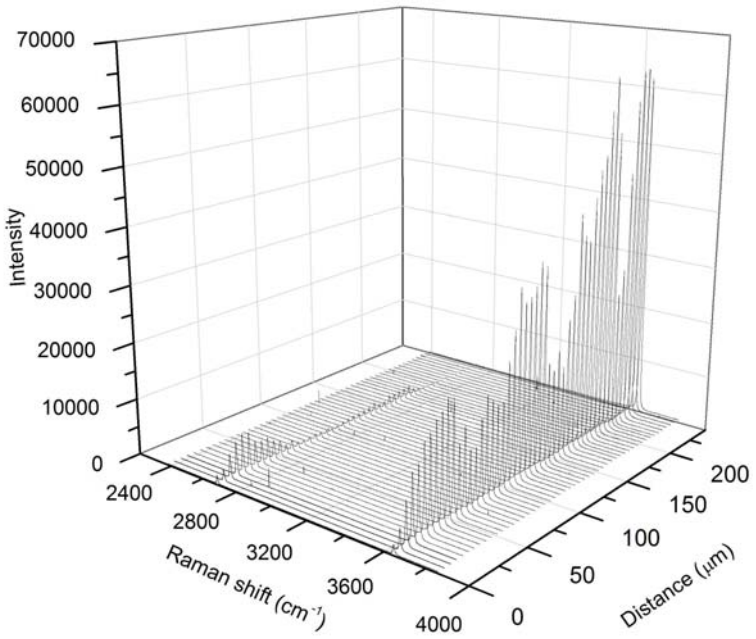

Figure 6. Guo et al.

This is a preprint, the final version is subject to change, of the American Mineralogist (MSA)
Cite as Authors (Year) Title. American Mineralogist, in press.
(DOI will not work until issue is live.) DOI: http://dx.doi.org/10.2138/am.2013.4550

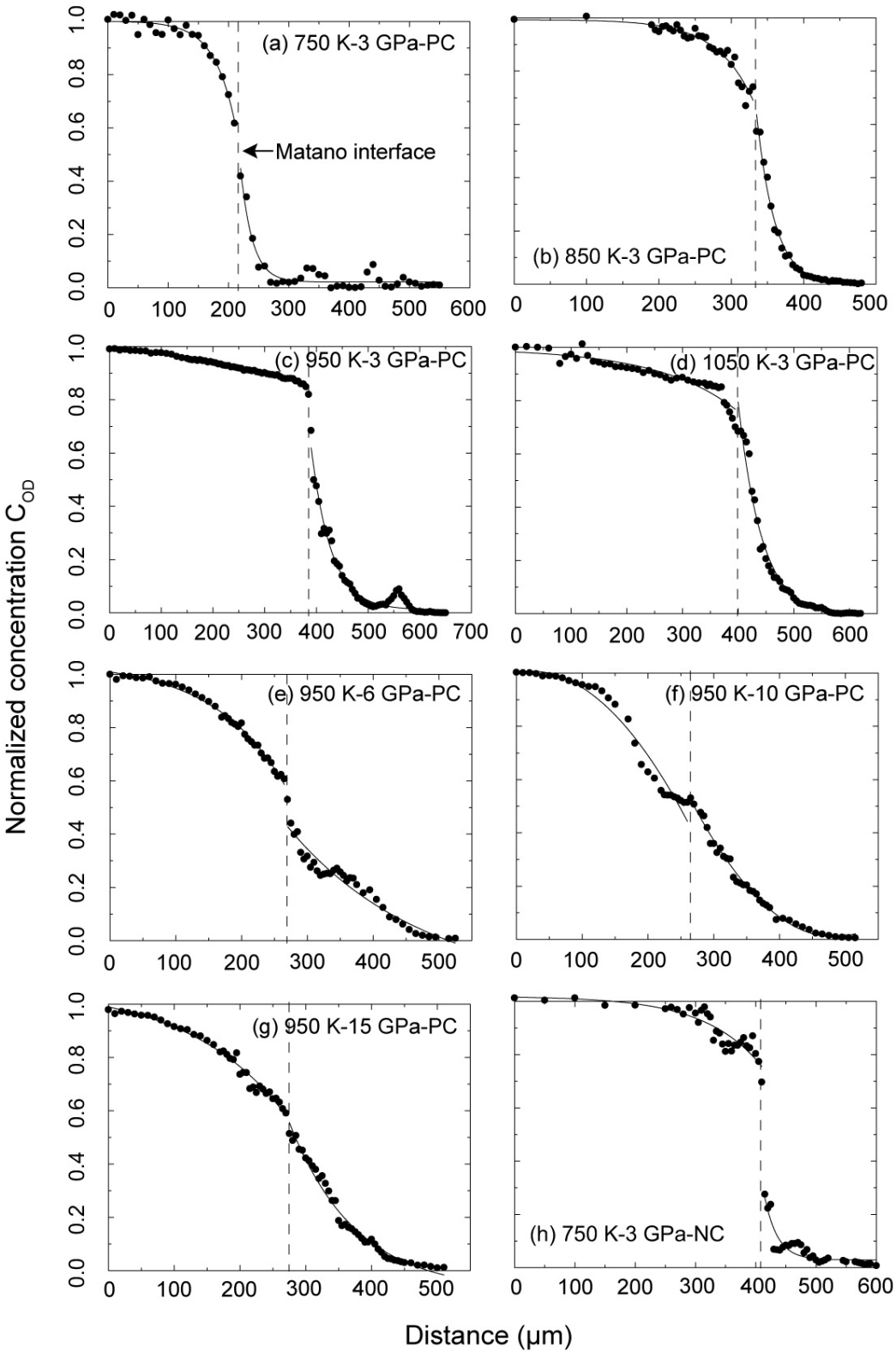

697

This is a preprint, the final version is subject to change, of the American Mineralogist (MSA)
Cite as Authors (Year) Title. American Mineralogist, in press.
(DOI will not work until issue is live.) DOI: http://dx.doi.org/10.2138/am.2013.4550

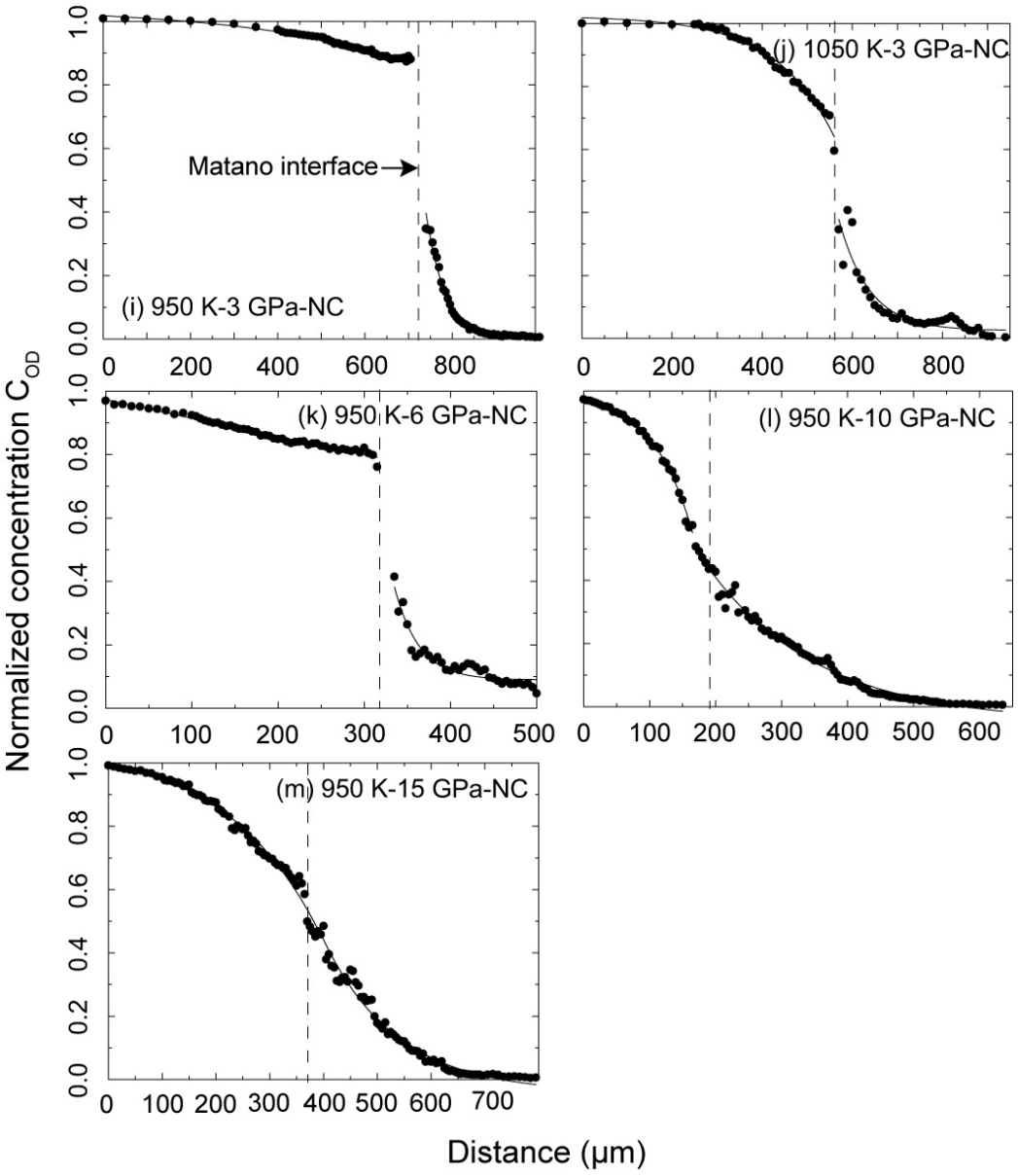

698

699 Figure 7. Guo et al.

700

This is a preprint, the final version is subject to change, of the American Mineralogist (MSA)
Cite as Authors (Year) Title. American Mineralogist, in press.
(DOI will not work until issue is live.) DOI: http://dx.doi.org/10.2138/am.2013.4550

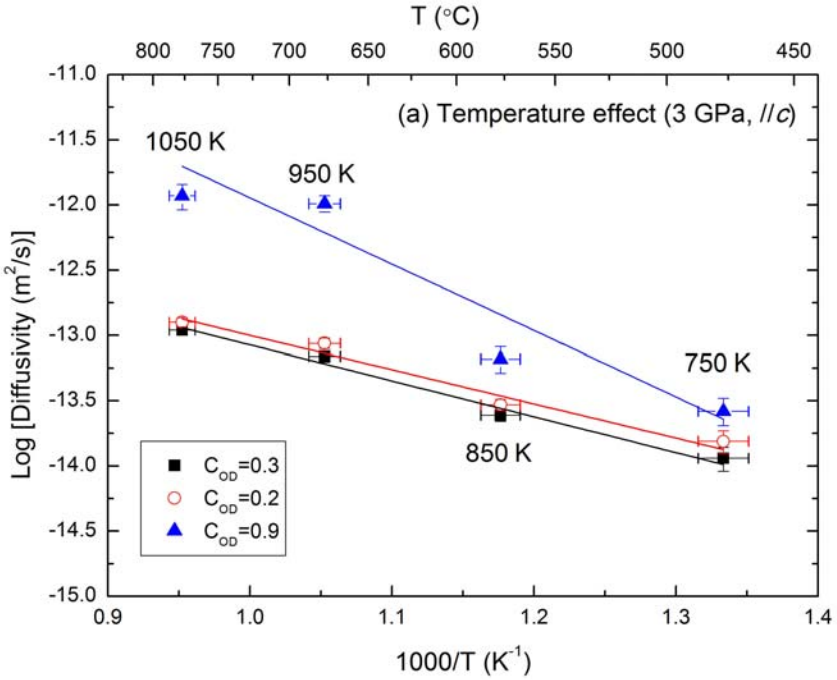

701

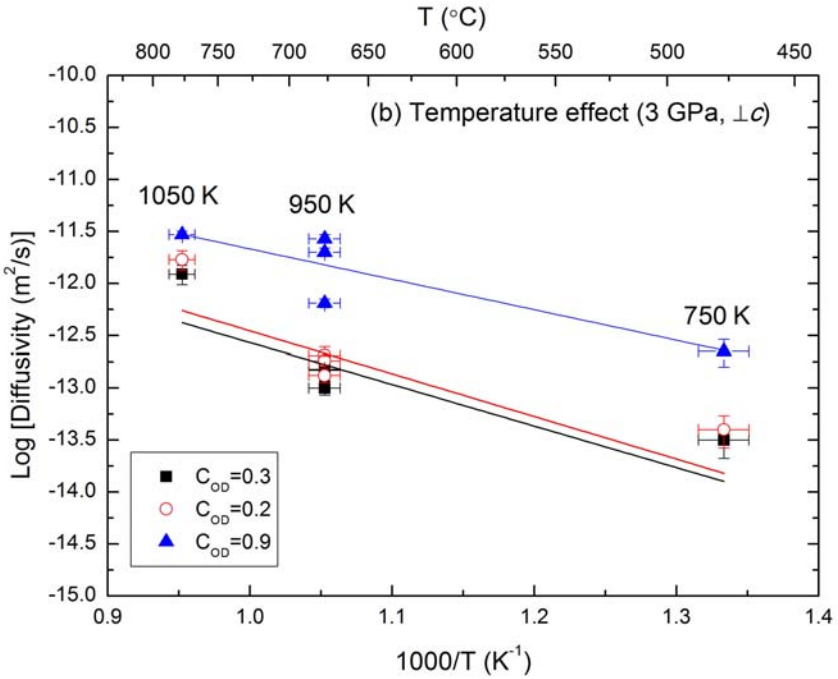

702

703

704 Figure 8. Guo et al.

705

706

This is a preprint, the final version is subject to change, of the American Mineralogist (MSA)
Cite as Authors (Year) Title. American Mineralogist, in press.
(DOI will not work until issue is live.) DOI: http://dx.doi.org/10.2138/am.2013.4550

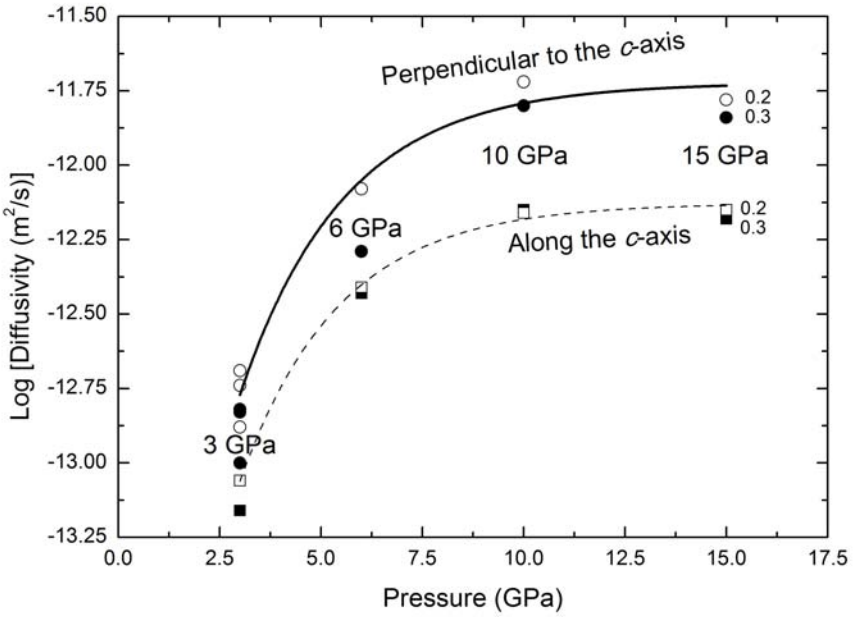

Figure 9. Guo et al.

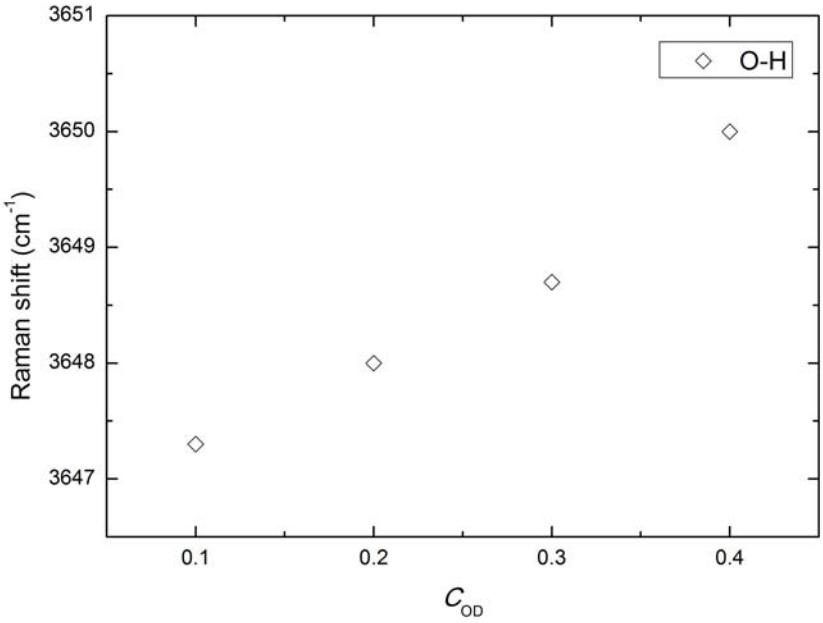

719

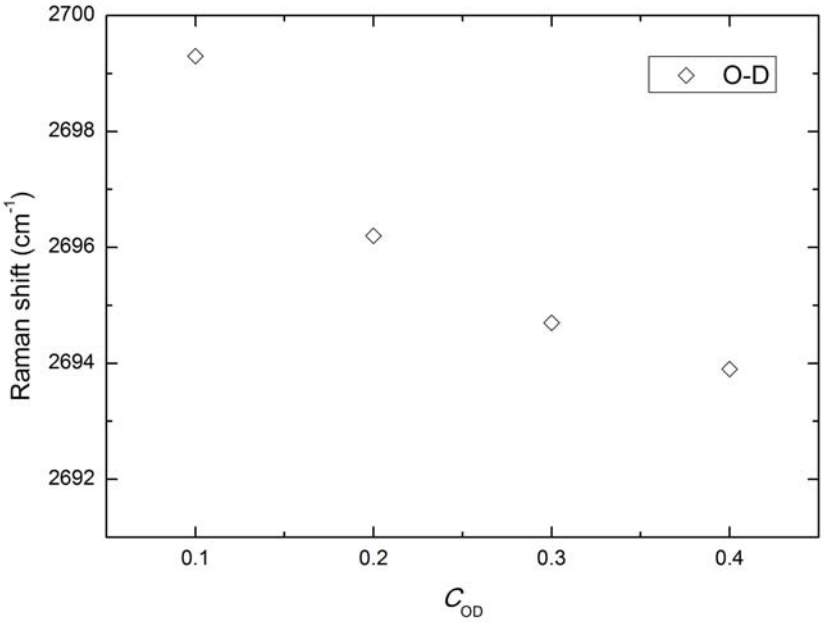

720

721

722 Figure 10. Guo et al.

723

724

725

This is a preprint, the final version is subject to change, of the American Mineralogist (MSA)
Cite as Authors (Year) Title. American Mineralogist, in press.
(DOI will not work until issue is live.) DOI: http://dx.doi.org/10.2138/am.2013.4550

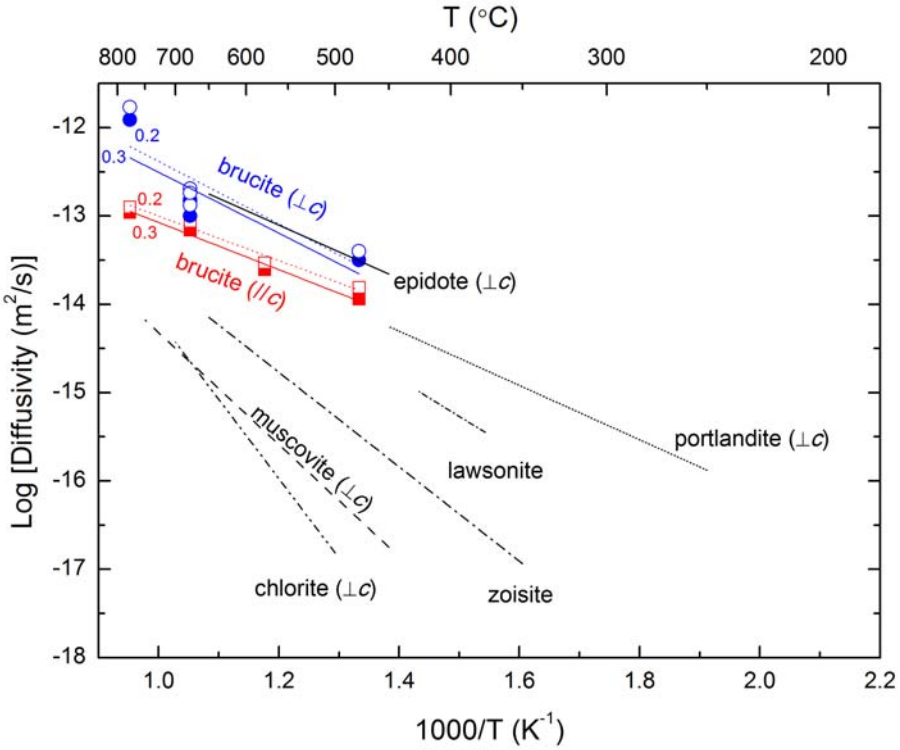

726

727 Figure 11. Guo et al.

728

729

730

Table 1. Experimental conditions and H-D interdiffusion coefficients

Run no.	Orientation	P (GPa)	T (K)	Duration (h)	Capsule	Log D(m^2/s) (C_{OD}=0.3)	Log D(m^2/s) (C_{OD}=0.2)	Log D(m^2/s) (C_{OD}=0.9)
A2338	//*c* axis	3	750	0	Au	-	-	-
A2315	//*c* axis	3	750	15	Pt	$-13.94(^{+0.08}_{-0.10})$	$-13.81(^{+0.08}_{-0.10})$	$-13.19^{+0.10}_{-0.11}$
A2336	//*c* axis	3	850	7	Pt	$-13.61(^{+0.04}_{-0.05})$	$-13.53(^{+0.04}_{-0.04})$	$-13.18(^{+0.10}_{-0.11})$
A2349	//c axis	3	950	6.3	Au	$-13.16(^{+0.04}_{-0.04})$	$-13.06(^{+0.04}_{-0.04})$	$-11.99(^{+0.09}_{-0.10})$
A2351	//c axis	3	1050	4.3	Au	$-12.96(^{+0.04}_{-0.04})$	$-12.9(^{+0.03}_{-0.04})$	$-11.93(^{+0.09}_{-0.11})$
1K1569	//c axis	6	950	6	Pt	$-12.43(^{+0.12}_{-0.13})$	$-12.41(^{+0.12}_{-0.13})$	$-12.52(^{+0.03}_{-0.03})$
1K1571	//c axis	10	950	2	Pt	$-12.15(^{+0.04}_{-0.05})$	$-12.16(^{+0.04}_{-0.05})$	$-12.27(^{+0.22}_{-0.24})$
1K1543	//c axis	15	950	2	Pt	$-12.18(^{+0.03}_{-0.04})$	$-12.15(^{+0.03}_{-0.04})$	$-11.89(^{+0.04}_{-0.05})$
5K1918	c axis	3	750	5.5	Pt	$-13.50(^{+0.13}_{-0.18})$	$-13.40(^{+0.13}_{-0.18})$	$-12.65(^{+0.12}_{-0.15})$
5K1917	c axis	3	1050	1	Pt	$-11.91(^{+0.08}_{-0.10})$	$-11.77(^{+0.08}_{-0.10})$	$-11.53(^{+0.03}_{-0.04})$
5K1911	c axis	3	950	11	Pt	$-12.83(^{+0.08}_{-0.10})$	$-12.69(^{+0.08}_{-0.10})$	$-12.19(^{+0.04}_{-0.04})$
5K1912	c axis	3	950	1	Pt	$-13.00(^{+0.06}_{-0.07})$	$-12.88(^{+0.06}_{-0.07})$	$-11.57(^{+0.04}_{-0.04})$

A2364	c axis	3	950	4	Pt	$-12.82(^{+0.04}_{-0.05})$	$-12.74(^{+0.04}_{-0.05})$	$-11.7(^{+0.04}_{-0.04})$
1K1492	c axis	6	950	1.2	Pt	$-12.29(^{+0.06}_{-0.07})$	$-12.08(^{+0.06}_{-0.07})$	$-11.3(^{+0.04}_{-0.05})$
1K1487	c axis	10	950	2	Pt	$-11.80(^{+0.06}_{-0.07})$	$-11.72(^{+0.06}_{-0.07})$	$-12.15(^{+0.03}_{-0.03})$
1K1469	c axis	15	950	2	Pt	$-11.84(^{+0.07}_{-0.08})$	$-11.78(^{+0.07}_{-0.08})$	$-11.68(^{+0.03}_{-0.03})$